

The following resources related to this article are available online at www.sciencemag.org (this information is current as of September 1, 2009):

Updated information and services, including high-resolution figures, can be found in the online version of this article at:

<http://www.sciencemag.org/cgi/content/full/325/5943/985>

Supporting Online Material can be found at:

<http://www.sciencemag.org/cgi/content/full/325/5943/985/DC1>

A list of selected additional articles on the Science Web sites **related to this article** can be found at:

<http://www.sciencemag.org/cgi/content/full/325/5943/985#related-content>

This article **cites 28 articles**, 2 of which can be accessed for free:

<http://www.sciencemag.org/cgi/content/full/325/5943/985#otherarticles>

This article has been **cited by** 1 articles hosted by HighWire Press; see:

<http://www.sciencemag.org/cgi/content/full/325/5943/985#otherarticles>

This article appears in the following **subject collections**:

Geochemistry, Geophysics

http://www.sciencemag.org/cgi/collection/geochem_phys

Information about obtaining **reprints** of this article or about obtaining **permission to reproduce this article** in whole or in part can be found at:

<http://www.sciencemag.org/about/permissions.dtl>

The observed spatial and spectral variations in the photon imaging of the Ag chain (Figs. 3C and 4B) are dominated by the LDOS of the Ag₁₀ chain, as described by Eq. 4, and coupling to the plasmons serves to strengthen the emitted light intensity. Because of the relative spatial uniformity of the initial state, the emitted light intensity is highlighted by the gradient of the final state, $\frac{dV_f}{dx}$. In (7), the data led to the conclusion that light emission is caused by the coupling of the initial state $|i\rangle$ and final state $|f\rangle$ via the IET process, $\langle i|\mathbf{V}|f\rangle$, where \mathbf{V} is the interaction potential. In our experiment, it is refined by Fermi's golden rule, in which $|i\rangle$ and $|f\rangle$ are connected by the momentum operator \mathbf{p} , as $\langle i|\mathbf{p}|f\rangle$. This refinement and the association of \mathbf{V} with \mathbf{p} are not revealed by spectroscopy at discrete points as in (7). The transition still goes through the same initial and final states, but the momentum operator in the matrix element gives rise to the seemingly surprising spatial images.

Although only results from Ag₁₀ are presented here, the correspondence between nodes and emission maxima was also observed for Ag₂ through Ag₉. The wave functions for the particle-in-a-box-like atomic chains are simple and exhibit distinct features in energy and space, most notably the nodal structures. By varying the bias

voltage to control tunneling electrons and the radiative transition in inelastic tunneling, the STM is used to obtain spatially and spectrally resolved photon images that lead to direct visualization of Fermi's golden rule, one of the fundamental principles in quantum mechanics. In addition, these results reveal the basic mechanisms underlying optical phenomena at the nanoscale, where light fields with wavelengths much greater than the dimension of the radiator are enhanced by coupling to plasmons.

References and Notes

1. M. F. Crommie, C. P. Lutz, D. M. Eigler, *Nature* **363**, 524 (1993).
2. H. C. Manoharan, C. P. Lutz, D. M. Eigler, *Nature* **403**, 512 (2000).
3. N. Niluis, T. M. Wallis, W. Ho, *Science* **297**, 1853 (2002).
4. T. M. Wallis, N. Niluis, W. Ho, *Phys. Rev. Lett.* **89**, 236802 (2002).
5. X. H. Qiu, G. V. Nazin, W. Ho, *Science* **299**, 542 (2003).
6. S. W. Wu, G. V. Nazin, W. Ho, *Phys. Rev. B* **77**, 205430 (2008).
7. G. V. Nazin, X. H. Qiu, W. Ho, *Phys. Rev. Lett.* **90**, 216110 (2003).
8. R. Berndt *et al.*, *Phys. Rev. Lett.* **74**, 102 (1995).
9. R. Berndt *et al.*, *Science* **262**, 1425 (1993).
10. G. Schull, M. Becker, R. Berndt, *Phys. Rev. Lett.* **101**, 136801 (2008).
11. The details of this experiment are available as supporting material on *Science Online*.
12. R. Berndt, J. K. Gimzewski, P. Johansson, *Phys. Rev. Lett.* **67**, 3796 (1991).

13. P. Johansson, R. Monreal, P. Apell, *Phys. Rev. B* **42**, 9210 (1990).
14. K. Meguro, K. Sakamoto, R. Arafune, M. Satoh, S. Ushioda, *Phys. Rev. B* **65**, 165405 (2002).
15. B. C. Stipe, M. A. Rezaei, W. Ho, *Science* **280**, 1732 (1998).
16. R. Berndt, J. K. Gimzewski, *Phys. Rev. B* **48**, 4746 (1993).
17. J. Yan, Z. Yuan, S. Gao, *Phys. Rev. Lett.* **98**, 216602 (2007).
18. S. A. Maier, H. A. Atwater, *J. Appl. Phys.* **98**, 011101 (2005).
19. G. Hoffmann, L. Libioule, R. Berndt, *Phys. Rev. B* **65**, 212107 (2002).
20. N. Niluis, T. M. Wallis, W. Ho, *J. Phys. Chem.* **109**, 20657 (2005).
21. G. C. Schatz, M. A. Ratner, *Quantum Mechanics in Chemistry* (Dover, New York, 2002), chap. 4 and 5.
22. S. C. Lui, M. H. Kang, E. J. Mele, E. W. Plummer, D. M. Zehner, *Phys. Rev. B* **39**, 13149 (1989).
23. Supported by the Chemical Science, Geo- and Bioscience Division, Office of Science, U. S. Department of Energy, under grant DE-FG02-04ER1595, and by the Alexander von Humboldt Foundation through a Feodor Lynen Fellowship to C.A.B. We thank R. Wu, D. L. Mills, P. Chu, Y. Jiang, and N. Ogawa for inspiring discussions.

Supporting Online Material

www.sciencemag.org/cgi/content/full/325/5943/981/DC1
Materials and Methods
Fig. S1

6 April 2009; accepted 26 June 2009
10.1126/science.1174592

Homogeneous Distribution of ²⁶Al in the Solar System from the Mg Isotopic Composition of Chondrules

Johan Villeneuve,^{1*} Marc Chaussidon,¹ Guy Libourel^{1,2}

The timing of the formation of the first solids in the solar system remains poorly constrained. Micrometer-scale, high-precision magnesium (Mg) isotopic analyses demonstrate that Earth, refractory inclusions, and chondrules from primitive meteorites formed from a reservoir in which short-lived aluminum-26 (²⁶Al) and Mg isotopes were homogeneously distributed at $\pm 10\%$. This level of homogeneity validates the use of ²⁶Al as a precise chronometer for early solar system events. High-precision chondrule ²⁶Al isochrons show that several distinct chondrule melting events took place from ~ 1.2 million years (My) to ~ 4 My after the first solids condensed from the solar nebula, with peaks between ~ 1.5 and ~ 3 My, and that chondrule precursors formed as early as $0.87^{+0.19}_{-0.16}$ My after.

Models of the evolution of the early solar system rely on knowledge of the precise time scales for the physical and chemical processes that occurred in the early accretion disk and led to the formation of calcium-aluminum-rich inclusions (CAIs) and chondrules, which are the building blocks of

primitive meteorites (chondrites). Short-lived ²⁶Al [half-life ($T_{1/2}$) = 0.73 million years (My)] is possibly the most accurate chronometer for the first few million years of solar system history, provided that it was homogeneously distributed in the disk. Previous studies of various meteoritic components showed that ²⁶Al was widespread in the disk, but its level of homogeneity has never been quantified precisely. From numerous mineral ²⁶Al isochrons in CAIs, a canonical value of $\sim 5 \times 10^{-5}$ was inferred for the initial ²⁶Al/²⁷Al ratio [hereafter (²⁶Al/²⁷Al)₀] when CAIs crystallized (t). This value is slightly lower than $5.23 (\pm 0.13) \times 10^{-5}$, which was determined from the bulk ²⁶Al isochron of

Allende CAIs (2) [used in our work instead of $5.85 (\pm 0.05) \times 10^{-5}$ (3)], which indicates that the crystallization of CAIs followed closely after (50,000 years at most) the condensation of their precursors. The bulk ²⁶Al isochron precisely defines an initial Mg isotopic composition ($\delta^{26}\text{Mg}^*_0$) for CAI precursors of -0.040 ± 0.029 per mil (‰) (2). If ²⁶Al and Mg isotopes were homogeneously distributed in the inner solar system, then CAIs $\delta^{26}\text{Mg}^*_0$ can be taken as the initial Mg isotopic composition of the solar system when ²⁶Al/²⁷Al was $5.23 (\pm 0.13) \times 10^{-5}$. Any object that formed later (when ²⁶Al/²⁷Al < 5.23×10^{-5}) must be characterized by a more radiogenic $\delta^{26}\text{Mg}^*_0$ value. The increase of $\delta^{26}\text{Mg}^*_0$ is a function of the Al/Mg ratio of the reservoir in which the object, or its precursors, resided before the last melting event. Al-rich and ferromagnesian chondrules from unequilibrated ordinary chondrites (UOCs) and carbonaceous chondrites (CCs) show mineral ²⁶Al isochrons with (²⁶Al/²⁷Al)₀ < 2×10^{-5} (4–12); that is, much lower than that of CAIs. Because the $\delta^{26}\text{Mg}^*_0$ of chondrules has never been precisely determined, the data from chondrules cannot be compared to those of CAIs nor to the theoretical Mg isotope growth curve calculated for the solar nebula for a homogeneous distribution of ²⁶Al and Mg isotopes.

We developed high-precision analysis of Al and Mg isotopes using the Centre de Recherches Petrographiques et Geochimiques (CRPG)–CNRS Cameca ion microprobe (ims 1270) to determine precisely (even for low Al/Mg ratios)

¹Centre de Recherches Petrographiques et Geochimiques (CRPG)–Nancy Université–CNRS, UPR 2300, 15 Rue Notre-Dame des Pauvres, Boîte Postale 20, 54501 Vandoeuvre-lès-Nancy, France. ²Ecole Nationale Supérieure de Géologie (ENSG)–Nancy Université, Rue du Doyen Marcel Roubault, Boîte Postale 40, 54501 Vandoeuvre-lès-Nancy, France.

*To whom correspondence should be addressed. E-mail: johanv@crpg.cnrs-nancy.fr

both the slope [from which comes access to $(^{26}\text{Al}/^{27}\text{Al})_0$] and the intercept ($\delta^{26}\text{Mg}^*_0$) of mineral ^{26}Al isochrons in chondrules. We performed multicollection analyses of ^{24}Mg , ^{25}Mg , ^{26}Mg , and ^{27}Al using four Faraday cups (figs. S1 and S2) (13) in the major silicate phases (olivine, low-Ca pyroxene, and mesostasis) of 15 chondrules [three type I (FeO-poor), 11 type II (FeO-rich), and one Al-rich] from the LL3.0 UOC Semarkona. A typical external reproducibility of $\pm 0.005\%$ (2σ) can be obtained for $\delta^{26}\text{Mg}^*$ in magnesium silicate standards (fig. S2) (13). In chondrules, internal errors (2σ) for $\delta^{26}\text{Mg}^*$ were $\pm 0.015\%$ to $\pm 1.98\%$, depending on Mg content (table S1).

The 14 ferromagnesian chondrules show well-resolved mineral isochrons (two examples are shown in Fig. 1, with the remainder shown in fig. S4), with $(^{26}\text{Al}/^{27}\text{Al})_0$ ranging from $1.619 (\pm 0.167) \times 10^{-5}$ to $3.023 (\pm 1.240) \times 10^{-6}$ and $\delta^{26}\text{Mg}^*_0$ values ranging from $-0.0185 (\pm 0.0140)\%$ to $0.0047 (\pm 0.0098)\%$ for Sem-Ch138, Sem-Ch83, and Sem-Ch121, respectively (table S1). Because most Mg-rich olivines in type I chondrules might not have crystallized from the chondrule melt (14, 15), it is theoretically not correct to calculate an isochron between olivine and glass in Sem-Ch2. The $(^{26}\text{Al}/^{27}\text{Al})_0$ for Sem-Ch2 can, however, be determined precisely (fig. S4). The Al-rich chondrule (Sem-Ch4) shows constant ^{26}Mg excesses [$\delta^{26}\text{Mg}^* = 0.098 (\pm 0.016)\%$,

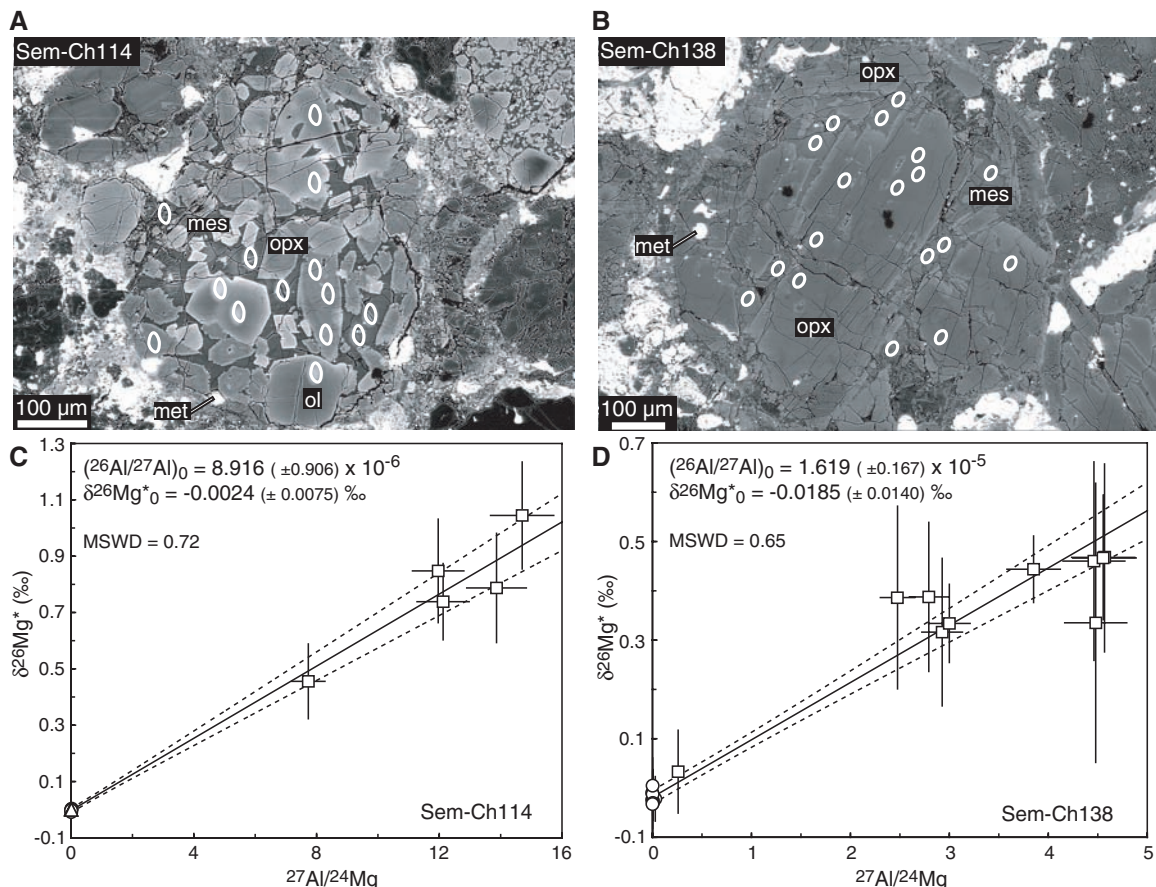
fig. S4] that are not correlated with Al/Mg ratio but would indicate that the last melting event occurred at least 4 My after CAIs; that is, when $(^{26}\text{Al}/^{27}\text{Al})_0 < 10^{-6}$.

Because of their high precision, the present chondrule Al-Mg data can be compared to the growth curve calculated for Mg isotopes in the solar nebula, assuming a simple closed-system evolution (Fig. 2). If ^{26}Al and Mg isotopes were homogeneously distributed in the nebula, any chondrule formed at a given time t , from precursors extracted from the nebula at that time, must have $(^{26}\text{Al}/^{27}\text{Al})_0$ and $\delta^{26}\text{Mg}^*_0$ identical to those of the nebula growth curve at time t . The present ferromagnesian chondrules do plot, within errors, on the solar nebula growth curve, on which Earth also plots (Fig. 2), implying a homogenous distribution of ^{26}Al and Mg isotopes in the inner solar nebula at the time of formation of CAIs. The clustering of chondrule data along the solar nebula growth curve implies a relative heterogeneity of $\sim \pm 10\%$ (that is, $\pm 0.5 \times 10^{-5}$ for $^{26}\text{Al}/^{27}\text{Al}$ ratios and $\pm 0.004\%$ for $\delta^{26}\text{Mg}^*$, fig. S5). However, this is an upper bound, because part of the chondrule variability may be due to the following: (i) different closed-system evolution paths for up to ~ 1 My with bulk $^{27}\text{Al}/^{24}\text{Mg}$ slightly different from chondritic ratio and (ii) the possible presence within chondrule precursors of CAI-type material. One-million-year-old CAIs would have a bulk

$\delta^{26}\text{Mg}^*$ of $\sim -0.42\%$ (for a bulk $^{27}\text{Al}/^{24}\text{Mg}$ of 2), implying that their fraction in chondrule precursors could not be higher than $\sim 1\%$ (that is, $0.004/0.42$). Finally, it can be seen from Fig. 2 that the bulk ^{26}Al isochron for CAIs with $(^{26}\text{Al}/^{27}\text{Al})_0 = 5.85 (\pm 0.05) \times 10^{-5}$ and $\delta^{26}\text{Mg}^*_0 = -0.0317 (\pm 0.0038)\%$ (3) is not consistent with a homogeneous distribution of ^{26}Al , because that conclusion would imply a positive terrestrial $\delta^{26}\text{Mg}^*$ value of $\sim -0.015\%$ (16), and is not consistent with most of our chondrule data.

The ^{26}Al and Mg isotopic homogeneity of the solar system inferred from our data are not in conflict with the existence of supracanonical $^{26}\text{Al}/^{27}\text{Al}$ ratios (up to 7×10^{-5}) (17) or of large $\delta^{26}\text{Mg}^*$ variations in hibonites (up to 4%) (18). A variability of $\pm 0.5 \times 10^{-5}$ for $^{26}\text{Al}/^{27}\text{Al}$ ratio simply implies that the fraction of components having supra-canonical ratios within CAIs and chondrules precursors was less than $\sim 7\%$. Similarly, a variability of $\pm 0.004\%$ for $\delta^{26}\text{Mg}^*$ implies that the fraction of hibonite-type material was less than $\sim 0.1\%$. In such a homogeneous accretion disk, the composition of the Al-rich chondrule can be simply understood as the result of an earlier extraction of its precursors from the nebula followed by a protracted closed-system evolution until the last melting event. A closed-system evolution model based on the bulk $^{27}\text{Al}/^{24}\text{Mg}$ ratio of the Al-rich chon-

Fig. 1. (A and B) Back-scattered electron image of two Semarkona type II chondrules: porphyritic olivine-pyroxene chondrule Sem-Ch114 and porphyritic pyroxene chondrule Sem-Ch138 (white circles show ion probe spots). The major mineral phases are olivine (ol), low-Ca pyroxene (opx) surrounded by glassy mesostasis (mes), and a few Fe-Ni metal grains (met). **(C and D)** Isochron diagrams obtained from 14 and 18 ion probe analyses, respectively (open circles are for low-Ca pyroxene, open triangles for olivine, and the open square for mesostasis, plotted with 2σ error bars) (fig. S4, table S1) (13).



drule (determined at 0.70 from chemical mapping by secondary electron microscopy) implies that its precursors were extracted from the nebula $\sim 0.87^{+0.19}_{-0.16}$ My after CAIs (Fig. 2). This could have happened earlier if the precursors did not remain as a closed system for Al and Mg and if,

for example, Mg was added to the precursors by condensation, as has been proposed for Al-rich chondrules (19). For the ferromagnesian chondrules, which have $^{27}\text{Al}/^{24}\text{Mg}$ ratios close to the chondritic ratio (0.10 to 0.23 for our 13 chondrules), it is not possible to identify an early ex-

traction of their precursors (for example, 1 My earlier) from the present data (with an error of ± 0.01 to $\pm 0.02\%$ on $\delta^{26}\text{Mg}^*$), because their evolution in a closed system before melting would overlap, within errors, with the solar nebula growth curve.

Fig. 2. Solar system growth curve (solid line) of Mg isotopes anchored by the $(^{26}\text{Al}/^{27}\text{Al})_0$ and $\delta^{26}\text{Mg}^*_0$ of bulk CAIs [red square, $5.23 (\pm 0.13) \times 10^{-5}$ and $-0.040 (\pm 0.029)\%$] (2) and calculated for a chondritic $^{27}\text{Al}/^{24}\text{Mg}$ ratio of 0.101 (30). The green field corresponds to the growth curve that could be calculated from the bulk CAIs isochron of $5.85 (\pm 0.05) \times 10^{-5}$ and $-0.0317 (\pm 0.0038)\%$ (green square) (3). All ferromagnesian chondrules (colored diamonds) plot on the solar nebula growth curve and define an error envelope (in red) at $\pm 0.5 \times 10^{-5}$ for $^{26}\text{Al}/^{27}\text{Al}$ ratios and $\pm 0.004\%$ for $\delta^{26}\text{Mg}^*$ (red arrows). Type I Sem-Ch2 is not shown, because its $\delta^{26}\text{Mg}^*_0$ cannot be determined precisely (fig. S4). The steep solid line (and its blue error envelope) show how a model age can be calculated for the extraction from the nebula of the precursors of the Al-rich chondrule (blue diamond) using its bulk $^{27}\text{Al}/^{24}\text{Mg}$ ratio of 0.7. Two sigma error bars are shown.

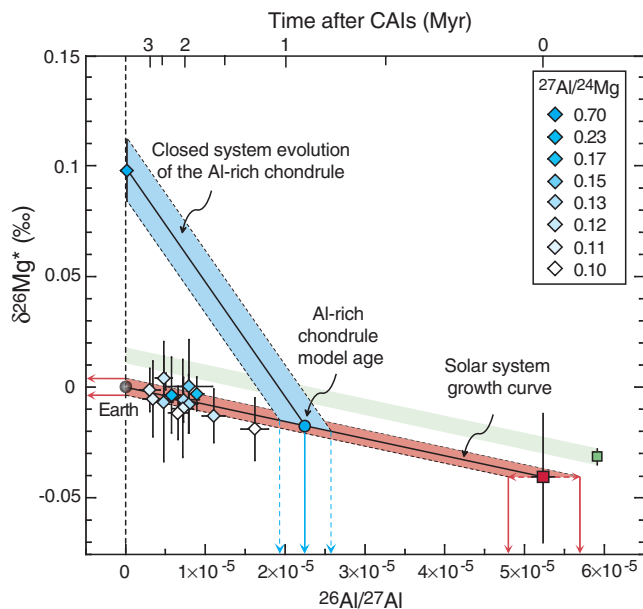
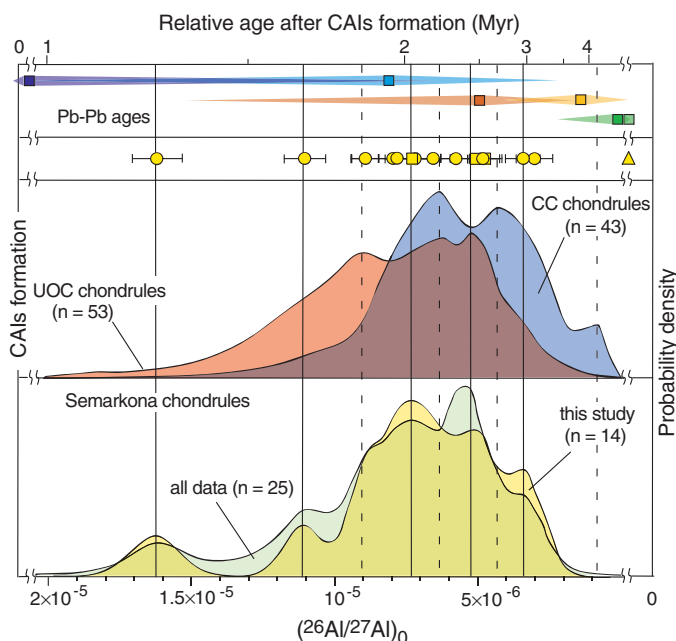


Fig. 3. $(^{26}\text{Al}/^{27}\text{Al})_0$ and corresponding relative ages after the formation of CAIs (2) determined for the 15 Semarkona chondrules (yellow squares for type I chondrules, yellow circles for type II chondrules, and yellow triangle for the Al-rich chondrule) compared with previous analyses of chondrules in the least-equilibrated ordinary and carbonaceous chondrites. Curves show probability density functions (n = number of data points in the distribution) of $(^{26}\text{Al}/^{27}\text{Al})_0$ in our Semarkona chondrules (yellow), all Semarkona chondrules (green), CC chondrules (blue), and UOC chondrules without our data (red). All data are available in table S2. Vertical solid lines show peaks that are present in Semarkona chondrules and often in UOC chondrules. Dotted lines show peaks that are present only in UOC chondrules and CC chondrules. The upper window corresponds to absolute Pb-Pb ages calculated from CV Allende chondrules (23) (dark and light blue squares), CR Acfer chondrules (20) (red and yellow squares), and CB Gujba (21) chondrules (dark and light green), depending on assumed age for CAIs (either 4567.2 ± 0.6 My or 4568.5 ± 0.5 My) (20, 22). One sigma error bar is shown.



Because ^{26}Al and Mg isotopes are homogeneously distributed in the inner solar system (within approximately $\pm 10\%$), different values of $(^{26}\text{Al}/^{27}\text{Al})_0$ among chondrules imply the existence of individual melting events at different times; for example, $\sim 1.77^{+0.66}_{-0.47}$ My between chondrule Sem-Ch138 and chondrule Sem-Ch83 (table S1). Our data can be used, in conjunction with data from previously published chondrules $(^{26}\text{Al}/^{27}\text{Al})_0$ (table S2), to investigate whether several major melting episodes can be identified or whether chondrule formation was a continuous process. Because data precision is variable, to make a meaningful comparison between all the data, we calculated a probability density distribution that sums the Gaussian distributions $f(^{26}\text{Al}/^{27}\text{Al})_{0,\sigma}$ calculated for each chondrule. The distribution of the 14 ferromagnesian Semarkona chondrules clearly shows five distinct episodes (Fig. 3) at 1.2, 1.6, 2.1, 2.4, and 2.9 My after CAIs [taking $(^{26}\text{Al}/^{27}\text{Al})_0$ for CAIs of 5.23×10^{-5}] (2). These five episodes are consistent with the $(^{26}\text{Al}/^{27}\text{Al})_0$ measured previously in 11 other Semarkona chondrules (Fig. 3 and table S2) (8, 10, 12); the two most prominent peaks in the distribution are at 2.1 and 2.4 My. Four other episodes of chondrule formation at 1.9, 2.2, 2.6, and 4.3 My can be tentatively identified considering all the available data for UOCs and CCs (Fig. 3 and table S2) (4–7, 9, 11). A Kolmogorov-Smirnov statistical test applied to these distributions confirms that the differences shown in Fig. 3 are statistically significant: The probability for the age distributions to be different between UOC and CC chondrules is 99%. In addition, even with only 25 chondrules, the age distribution of Semarkona chondrules is statistically the same as that of UOC chondrules (82%). Available Pb-Pb ages [from $0.6 (\pm 1.6)$ My to $5.8 (\pm 1.0)$ My after CAIs] (20–23) are consistent with ^{26}Al ages but not sufficiently precise to identify specific episodes of chondrule formation. The possible existence of a limited number of melting events over a few million years is a fundamental constraint to consider in models of chondrule formation.

The large scatter in the age distribution of chondrules (Fig. 3)—with $\sim 10\%$ of all chondrules formed between 0 and 1.5 My after CAIs, $\sim 40\%$ formed between 1.5 and 2.1 My, $\sim 40\%$ formed between 2.1 and 2.8 My, and $\sim 10\%$ formed beyond 2.8 My after CAIs—can be interpreted in two opposite ways: (i) the peak intensities reflect different magnitudes of chondrule formation at specific times and thus the major episodes of chondrule formation (for UOCs and CCs) would have taken place ~ 1.5 to ~ 3 My after CAIs; or (ii) the variable peak intensities reflect the poor efficiency of chondrule preserva-

tion in the accretion disk before the accretion of UOC and CC parent bodies. In the later scenario, chondrites would be enriched in chondrules formed shortly before accretion (which was constrained for H4 UOC at $^{26}\text{Al}/^{27}\text{Al} \approx 2 \times 10^{-7}$ from the metamorphic cooling of the parent body) (24). Although there is no evidence to favor one of these two extreme hypotheses over the other, it is obvious from the Al-rich chondrule that its precursors were extracted from the nebula $\sim 0.87^{+0.19}_{-0.16}$ My after CAIs and that they remained isolated in the nebula for up to ~ 3 My before chondrule formation. The presence of chondrules of different origins and different ages in the same few cubic centimeters of Semarkona is consistent with astrophysical models of the disk. Radial mixing by turbulence can efficiently distribute solids within 10 astronomical units in several tens of thousands of years, as long as these solids are small (millimeter or centimeter size) and are coupled to the gas (25), but the rate of destruction of these solids by accretion either by the Sun or by forming planetesimals is unknown. The observed age distribution (Fig. 3) does not exclude an early intense period (~ 1 My after CAIs or even before) of chondrule formation (or extraction of chondrule precursors), as was suggested by high $^{26}\text{Al}/^{27}\text{Al}$ inferred from bulk analyses of chondrules (26–28).

Our results imply the following: (i) that ^{26}Al was efficiently homogenized (within $\sim \pm 10\%$) in the inner solar system, (ii) that no substantial ^{26}Al (in excess of $^{26}\text{Al}/^{27}\text{Al} = 5 \times 10^{-5}$) was produced in the disk after time “zero” as defined by the bulk isochron of CAIs, and (iii) that the ^{26}Al - ^{26}Mg systematic has a chronological significance. Nebular models do predict an efficient

homogenization of ^{26}Al at $\sim \pm 10\%$ in the case of an external seeding of the accretion disk with ^{26}Al injected by a nearby supernova (29). In the case of the production of ^{26}Al by irradiation, it is not clear that such a level of homogeneity can be reached, unless most of the irradiated material is evaporated before time zero.

References and Notes

- G. J. Macpherson, A. M. Davis, E. K. Zinner, *Meteoritics* **30**, 365 (1995).
- B. Jacobsen *et al.*, *Earth Planet. Sci. Lett.* **272**, 353 (2008).
- K. Thrane, M. Bizzarro, J. A. Baker, *Astrophys. J.* **646**, L159 (2006).
- T. Kunihiro, A. E. Rubin, K. D. McKeegan, J. T. Wasson, *Geochim. Cosmochim. Acta* **68**, 2947 (2004).
- K. Nagashima, A. N. Krot, M. Chaussidon, *Meteorit. Planet. Sci.* **42**, A115 (2007).
- N. Sugiura, A. N. Krot, *Meteorit. Planet. Sci.* **42**, 1183 (2007).
- E. Kurahashi, N. T. Kita, H. Nagahara, Y. Morishita, *Geochim. Cosmochim. Acta* **72**, 3865 (2008).
- I. D. Hutcheon, R. Hutchison, *Nature* **337**, 238 (1989).
- S. S. Russell, G. Srinivasan, G. R. Huss, G. J. Wasserburg, G. J. MacPherson, *Science* **273**, 757 (1996).
- N. T. Kita, H. Nagahara, S. Togashi, Y. Morishita, *Geochim. Cosmochim. Acta* **64**, 3913 (2000).
- S. Mostefaoui *et al.*, *Meteorit. Planet. Sci.* **37**, 421 (2002).
- N. G. Rudraswami, J. N. Goswami, B. Chattopadhyay, S. K. Sengupta, A. P. Thapliyal, *Earth Planet. Sci. Lett.* **274**, 93 (2008).
- Materials and methods are available as supporting material on Science Online.
- G. Libourel, A. N. Krot, *Earth Planet. Sci. Lett.* **254**, 1 (2007).
- M. Chaussidon, G. Libourel, A. N. Krot, *Geochim. Cosmochim. Acta* **72**, 1924 (2008).
- M. Chaussidon, M. Gounelle, *C. R. Geosci.* **339**, 872 (2007).
- E. D. Young *et al.*, *Science* **308**, 223 (2005).
- M.-C. Liu, K. D. McKeegan, A. M. Davis, *Lunar Planet. Sci. XXXVII*, 2428 (2006).
- H. Nagahara, N. T. Kita, K. Ozawa, Y. Morishita, *Geochim. Cosmochim. Acta* **72**, 1442 (2008).
- Y. Amelin, A. N. Krot, I. D. Hutcheon, A. A. Ulyanov, *Science* **297**, 1678 (2002).
- A. N. Krot, Y. Amelin, P. Cassen, A. Meibom, *Nature* **436**, 989 (2005).
- A. Bouvier *et al.*, *Geochim. Cosmochim. Acta* **71**, 1583 (2007).
- Y. Amelin, A. Krot, *Meteorit. Planet. Sci.* **42**, 1321 (2007).
- E. Zinner, C. Gopel, *Meteoritics* **27**, 311 (1995).
- D. Bockelee-Morvan, D. Gautier, F. Hersant, J. M. Hure, F. Robert, *Astron. Astrophys.* **384**, 1107 (2002).
- A. Galy, E. D. Young, R. D. Ash, R. K. O’Nions, *Science* **290**, 1751 (2000).
- M. Bizzarro, J. A. Baker, H. Haack, *Nature* **431**, 275 (2004).
- M. Bizzarro, J. A. Baker, H. Haack, *Nature* **435**, 1280 (2005).
- A. P. Boss, *Astrophys. J.* **660**, 1707 (2007).
- K. Lodders, *Astrophys. J.* **591**, 1220 (2003).
- We gratefully thank C. Rollion-Bard, D. Mangin, and M. Champenois for their implication and expertise in ion probe techniques; J. Ravaux and A. Kohler for their help with SEM analysis; and J. Marin and P. Burnard for their attentive rereading. Constructive comments by three anonymous reviewers and fruitful discussions with F. Robert and M. Gounelle were highly appreciated and greatly improved this manuscript. This work was funded by L’Agence Nationale de la Recherche grant ANR-08-BLAN-0260-02 T-Tauri, Chem, and European Research Council grant ERC 226846 Cosmochemical Exploration of the first two Million Years of the Solar System (CEMYSS). This is CRPG publication number 2001.

Supporting Online Material

www.sciencemag.org/cgi/content/full/325/5943/985/DC1
Materials and Methods
Figs. S1 to S5
Tables S1 to S2
References

23 March 2009; accepted 19 June 2009
10.1126/science.1173907

Adjoint Tomography of the Southern California Crust

Carl Tape,^{1*} Qinya Liu,² Alessia Maggi,³ Jeroen Tromp⁴

Using an inversion strategy based on adjoint methods, we developed a three-dimensional seismological model of the southern California crust. The resulting model involved 16 tomographic iterations, which required 6800 wavefield simulations and a total of 0.8 million central processing unit hours. The new crustal model reveals strong heterogeneity, including local changes of $\pm 30\%$ with respect to the initial three-dimensional model provided by the Southern California Earthquake Center. The model illuminates shallow features such as sedimentary basins and compositional contrasts across faults. It also reveals crustal features at depth that aid in the tectonic reconstruction of southern California, such as subduction-captured oceanic crustal fragments. The new model enables more realistic and accurate assessments of seismic hazard.

The objective of seismic tomography is to produce detailed three-dimensional (3D) images of Earth’s interior by minimizing the differences between simulated (or “synthetic”) seismograms and recorded (or “observed”) seismograms. Seismic tomography has been successful in producing images of Earth’s interior, such

as large-scale variations in the mantle (1, 2), subducting slabs (3), and mantle plumes (4). These tomographic studies adopt a simple 1D (layered) reference model (5), which allows for computationally inexpensive procedures within the minimization problem. Highly accurate numerical methods, such as the spectral-element method

(SEM), may now be used to compute synthetic seismograms at regional and global scales, allowing tomographers to start the minimization procedure with more realistic 3D initial models and simulations (6–9). We demonstrated in this study that these numerical methods may be exploited within the minimization problem by using adjoint methods (10–12). We refer to this procedure as “adjoint tomography” (13).

Southern California provides an excellent setting for the two-fold objective of fitting seismograms and characterizing the crust. The station coverage (fig. S2A), especially in the Los Angeles region, is one of the densest in the world. A detailed 3D seismological model of the southern California crust has been constructed from a

¹Seismological Laboratory, California Institute of Technology, Pasadena, CA 91125, USA. ²Department of Physics, University of Toronto, Ontario M5S 1A7, Canada. ³Institut de Physique du Globe, Université de Strasbourg, 67084 Strasbourg, France. ⁴Department of Geosciences and Program in Applied and Computational Mathematics, Princeton University, Princeton, NJ 08544, USA.

*To whom correspondence should be addressed. E-mail: carltape@gps.caltech.edu